ADVANCED ELECTRONIC MATERIALS Open Access
www.advelectronicmat.de

Emulation of Synaptic Plasticity in WO_3-Based Ion-Gated Transistors

Ramin Karimi Azari, Luan Pereira Camargo, José Ramón Herrera Garza, Liam Collins, Wan– Yu Tsai, Lariel Chagas da Silva Neres, Patrick Dang, Martin Schwellberger Barbosa, and Clara Santato**

Neuromorphic systems, inspired by the human brain, promise significant advancements in computational efficiency and power consumption by integrating processing and memory functions, thereby addressing the von Neumann bottleneck. This paper explores the synaptic plasticity of a WO_3-based ion-gated transistor (IGT) in [EMIM][TFSI] and a 0.1 mol L^{-1} LiTFSI in [EMIM][TFSI] for neuromorphic computing applications. Cyclic voltammetry (CV), transistor characteristics, and atomic force microscopy (AFM) force–distance (FD) profiling analyses reveal that Li^+ brings about ion intercalation, together with higher mobility and conductance, and slower response time (τ). WO_3 IGTs exhibit spike amplitude-dependent plasticity (SADP), spike number-dependent plasticity (SNDP), spike duration-dependent plasticity (SDDP), frequency-dependent plasticity (FDP), and paired-pulse facilitation (PPF), which are all crucial for mimicking biological synaptic functions and understanding how to achieve different types of plasticity in the same IGT. The findings underscore the importance of selecting the appropriate ionic medium to optimize the performance of synaptic transistors, enabling the development of neuromorphic systems capable of adaptive learning and real-time processing, which are essential for applications in artificial intelligence (AI).

1. Introduction

Neuromorphic computation, inspired by the human brain's parallel processing, integrates both data handling and decision-making in a single location, in contrast to von Neumann architecture's separate memory and processor setup. This integration aims to enable more efficient, real-time processing and learning, marking a significant step forward in computing technology.[1–3]

Neuromorphic computation not only streamlines processing but also consumes far less power than conventional systems for data transmission and processing. This is due to its brain-like architecture, which naturally consumes less power (the human brain is incredibly power-efficient, using roughly 20 watts), making it a more sustainable alternative in the computing world compared to modern supercomputers, which require ≈28 megawatts.[4–7] Biomimetic architectures, such as neuromorphic systems, are essential for advancing artificial intelligence by adopting spiking neural networks (SNNs), enabling them to learn and process information in a manner similar to the human brain.[8] They enhance AI performance and capability, supporting complex tasks like pattern recognition and sensory data interpretation while enabling simultaneous storage and processing in a single device.[5,9,10]

Over the past few years, there has been considerable progress in developing synaptic devices that imitate brain functions, specifically in learning and memory. These devices aim to

R. Karimi Azari, L. P. Camargo, J. R. H. Garza, L. C. da S. Neres, P. Dang, C. Santato
Engineering Physics
Polytechnique Montreal
2500 Ch. Polytechnique
Montréal, QC H3T 1J4, Canada
E-mail: ramin.karimi@polymtl.ca; clara.santato@polymtl.ca

The ORCID identification number(s) for the author(s) of this article can be found under https://doi.org/10.1002/aelm.202400807

DOI: 10.1002/aelm.202400807

L. P. Camargo
Department of Chemistry
State University of Londrina (UEL)
Londrina, PR 86057-970, Brazil

L. Collins, W. Yu Tsai
Oak Ridge National Laboratory
1 Bethel Valley Road, Oak Ridge, TN 37830, USA

L. C. da S. Neres
Institute of Chemistry
State University of São Paulo (UNESP)
Araraquara, SP 14801-970, Brazil

M. S. Barbosa
Institute of Chemistry
Federal University of Goiás (UFG)
Goiânia, GO 74690-900, Brazil

replicate the fundamental ability of synapses to adjust the strength of neural connections (i.e., synaptic plasticity)—a key mechanism in memory formation—and significant progress has been made in studying artificial synapses and simulating biological neurons.[5]

There are mainly two types of devices that can replicate the idea of connecting two neurons through a synapse: two-terminal devices, known as memristors, and three-terminal devices, known as transistors.[11–13] These devices can control output current based on their design and the material used, functioning as either a digital switch, abruptly altering the conductance of the channel, or as an analog switch, gradually adjusting the channel's conductance.[14]

One of the synaptic devices capable of demonstrating both memory and processing simultaneously is the ion-gated transistor.[15] Synaptic IGTs with three terminals and ionic liquid (IL) gating have been suggested as a promising method to mimic biological synapses. Recently, a variety of materials, including organic compounds, metal oxides (MO), carbon-based nanomaterials, single crystals, and 2D materials have been investigated for their potential use in these synaptic IGTs.[16] Through this design, the modulation of channel conductance can be achieved with greater efficiency.[13,14,17–19]

In an IGT artificial synapse, the channel conductance represents the synaptic weight of a biological synapse. Channel conductance or plasticity can vary based on several factors, including input pulse amplitude (spike amplitude-dependent plasticity, SADP), duration (spike duration-dependent plasticity, SDDP), interval (frequency-dependent plasticity, FDP), number of spikes (spike number-dependent plasticity, SNDP), and paired-pulse facilitation (PPF). This behavior is analogous to how the excitatory postsynaptic current (EPSC) in biological synapses changes in response to variations in presynaptic pulse activity.[20] This property allows the artificial synapse to mimic both short-term (STP) and long-term plasticity (LTP), along with learning and forgetting mechanisms of biological synapses.[19,21]

Tungsten trioxide (WO_3), an *n*-type metal oxide with a bandgap of ≈2.5 eV, is recognized by its applications in electrochromism, sensing, photocatalysis, and photoelectrochemistry. These applications typically benefit from high surface area mesoporous nanostructures, which facilitate the permeation of ionic media.[22,23] Extensive research is being conducted on metal-oxide thin film-based IGTs, which have broad applications in areas such as energy conversion and storage devices, low-power wearable electronics and bioelectronics, light-emitting diodes, and neuromorphic computing.[24–27]

The high surface area of the channel in IGTs that employ mesoporous nanostructured WO_3 thin films is expected to enhance the degree of doping. The doping mechanism may include not only 2D electrostatic and conventional 3D electrochemical faradaic doping, which involves the insertion and de-insertion of ions in the oxide lattice, but also a nonconventional form of electrochemical doping. This latter form, confined at the interface between the IL and the metal oxide, is especially relevant for ILs composed of relatively large ions that may not be able to insert into the oxide lattice.[28]

The diffusion barrier encountered by Li^+ in WO_3 is notably low, attributable to the diminutive size of the Li^+. This characteristic makes Li^+ a promising dopant for WO_3 IGTs. The intercalation and deintercalation of Li^+ in a mixed conductor channel could improve WO_3 IGT plasticity performance.[29,30]

Among the diverse range of synaptic devices, IGT transistors based on WO_3 have emerged as a promising candidate for the development of hardware neural networks specifically designed for analog computing in neuromorphic applications.[31–33]

However, certain fundamental attributes observed in biological synapses, such as spontaneous decay indicative of forgetting behavior, SADP, SNDP, SDDP, FDP, PPF, and the transition from STP to LTP have not yet been reported in a WO_3-based IGT.[34]

The structure of the electric double layer (EDL) at the interface between the IL and the IGT channel can be studied by AFM FD profiling. This technique measures the force between the AFM probe tip and the ionic layering of the interface, as the tip moves vertically. The ionic layering at various spots on the channel film surface can be measured *in operando* (in transistor operation) by observing the patterns created on FD curves.

In this work, we report on mesoporous nanostructured WO_3 thin film-based IGTs using different ion gating media, specifically ILs [EMIM][TFSI] and 0.1 mol L^{-1} LiTFSI in [EMIM][TFSI]. Following WO_3 film fabrication and device assembly, we conducted electrochemical characterization of the WO_3 films through cyclic voltammetry, complemented by *in operando* AFM FD characterization of the EDL at the interface between the ion gating medium and WO_3 film. This comprehensive approach allowed us to effectively evaluate the synaptic performance of the WO_3-based IGTs. Our findings indicate the potential of doping WO_3 channels with various cations for the hardware implementation of artificial synapses in analog computing and memory applications.

2. Results and Discussion

2.1. Material Characterizations

WO_3 films with a thickness of 200 nm were deposited on SiO_2 substrates using spin coating. AFM topography images of WO_3 films deposited on SiO_2 substrates (**Figure 1a–d**) reveal a surface composed of small particles. The root mean square (rms) roughness is estimated to be ≈3.0 ± 0.4 nm, as depicted in the height profile.

The scanning electron microscopy (SEM) images (**Figure 2a,b**) of the spin-coated WO_3 film display a homogeneous granular surface morphology, characterized by closely packed nanoparticles. This uniformity in film morphology is essential for achieving consistent and reliable transistor performance. The images reveal some degree of porosity in the film, with particles sizes ranging approximately from 20 to 50 nm, consistent with AFM measurements.

We investigated the surface area and porosity of the WO_3 films by Brunauer–Emmett–Teller (BET) analysis, critical for studying intercalation processes and ion mobility within the film. The mesoporous structure revealed by BET analysis indicates a high surface area (277 $m^2\ g^{-1}$), essential for efficient ion gating, particularly. The film's porosity (pore volume = 0.36 $cm^3\ g^{-1}$ and pore size = 4.4 nm) plays a key role in facilitating ionic mobility within the transistor channel, improving ion gating performance by enhancing ions accessibility, into the WO_3 lattice. This, in turn,

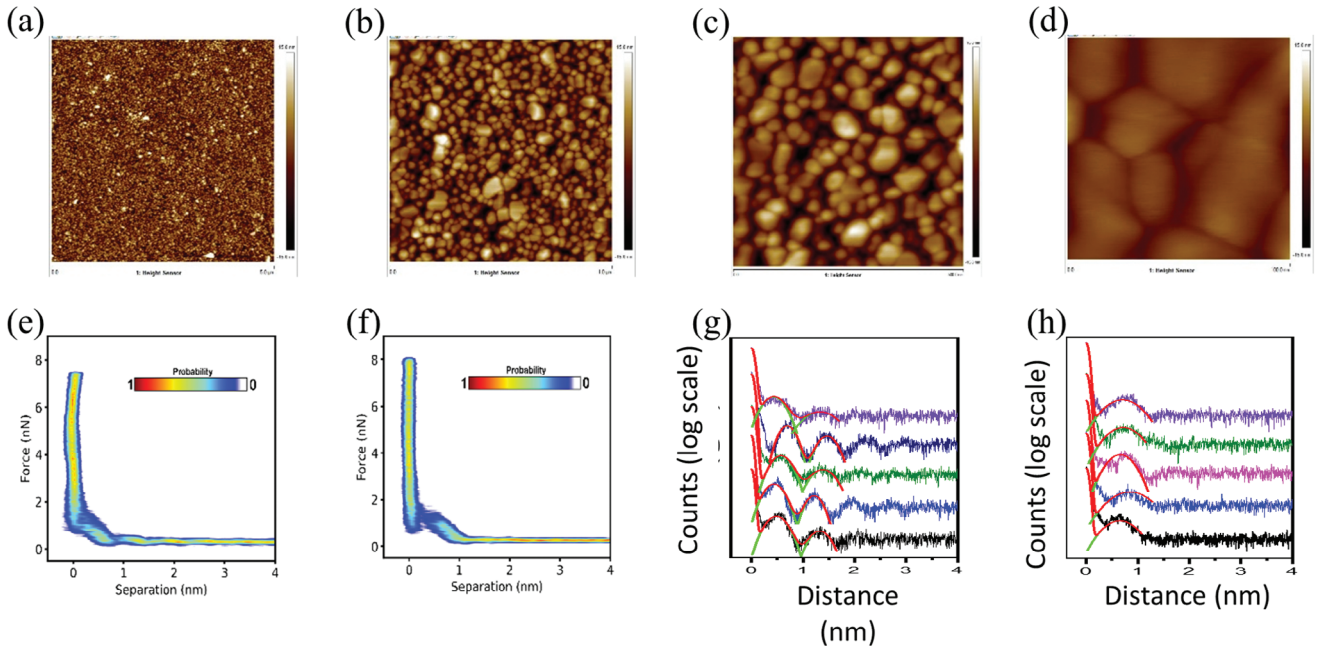

Figure 1. AFM height images of WO_3 films with size: a) 5 μm × 5 μm, b) 1 μm × 1 μm, c) 500 nm × 500 nm, d) 100 nm × 100 nm. 2D force-separation histogram from IL/WO_3 interface for WO_3 IGT based on e) [EMIM][TFSI] f) 0.1 mol L^{-1} LiTFSI in [EMIM][TFSI]. Separation histogram with Gaussian fitting g) for the peaks of five different spots in a WO_3 IGT with [EMIM][TFSI] h) for the peaks of five different spots in a WO_3 IGT with 0.1 mol L^{-1} LiTFSI in [EMIM][TFSI] gating material.

influences the device's channel current and response time (sizes of $EMIM^+$ and Li^+ measuring ≈0.7 and 0.07 nm).[35,36]

The structural properties of the WO_3 thin films were investigated using X-ray diffraction (XRD) (Figure 2b-inset). The diffraction pattern confirms the formation of a monoclinic WO_3 phase, with prominent peaks observed at 2θ values of ≈23°, 34°, and 49°, corresponding to the (002), (200), and (020) reflections, and a high degree of crystallinity of monoclinic WO_3 film (indexed to Joint Committee on Powder Diffraction Standards file #JCPDS 43–1035).

2.2. Cyclic voltammetry measurements of WO_3-based IGT

We analyzed the CVs of WO_3 thin films gated by two systems: pure [EMIM][TFSI] and a mixture of 0.1 mol L^{-1} LiTFSI in [EMIM][TFSI] at different scan rates (10, 50, and 100 mV s^{-1}) (Figure 2c,e). The CV of the WO_3 thin films gated with pure [EMIM][TFSI] shows distinct redox signals. However, in the presence of Li^+, the CV traces display broader signals with a higher voltametric current.

In previous works, we discussed that WO_3 IGTs gated by [EMIM][TFSI] undergo an interface-confined, unconventional chemical doping process, where large [EMIM] cations accumulate at the interface to compensate for the charge of the injected electrons. Conversely, in the presence of small cations such as Li^+, WO_3 undergoes an electrochemical doping process, where the cations are intercalated during the faradaic reduction via a double injection mechanism.[25]

In the absence of Li^+, the unconventional chemical doping mechanism dominates, with large [EMIM] cations accumulating at the interface to compensate for injected electrons, resulting in a sharper voltametric peak. Conversely, the presence of Li^+ enables a dual doping process, combining a conventional faradaic Li^+/e^- double injection with the interface-limited unconventional $[EMIM]^+$ doping. In the pure [EMIM][TFSI] system, redox reactions primarily involve the transfer of electrons in the WO_3 structure. When Li^+ is introduced, both electron and Li^+ injection must be considered ($WO_3 + ye^- + yLi^+ \leftrightarrow Li_yWO_3$). The additional charge injected via the Li^+/e^- double injection mechanism results in higher voltammetric currents in the CV.

2.3. Study of EDL at the interface of gating/channel material via AFM FD profiling

To gain a better understanding of the gating mechanisms and their relationship to the neuromorphic response, we studied *in operando* the structure of the electrical double layer (EDL) formed at the ion gating medium/WO_3 interface. The structure of the ion layering was characterized by AFM FD profiling in devices gated with both pure [EMIM][TFSI] and 0.1 mol L^{-1} LiTFSI in [EMIM][TFSI]. The devices were studied under a V_{gs} = 1 V to investigate the structure of the EDL associated to an advanced degree of doping. With the AFM tip was positioned in the middle of the channel, 50–100 individual force-distance curves were collected and the results were statistically analyzed using histograms to reveal the structural characteristics of the ionic layers at the WO_3/IL interface. Typical 2D histograms from the FD curves collected in pure [EMIM][TFSI] revealed distinguishable humps related to the first four-five ion layers (Figure 1e), consistent with our previous study of this type of device.[37]

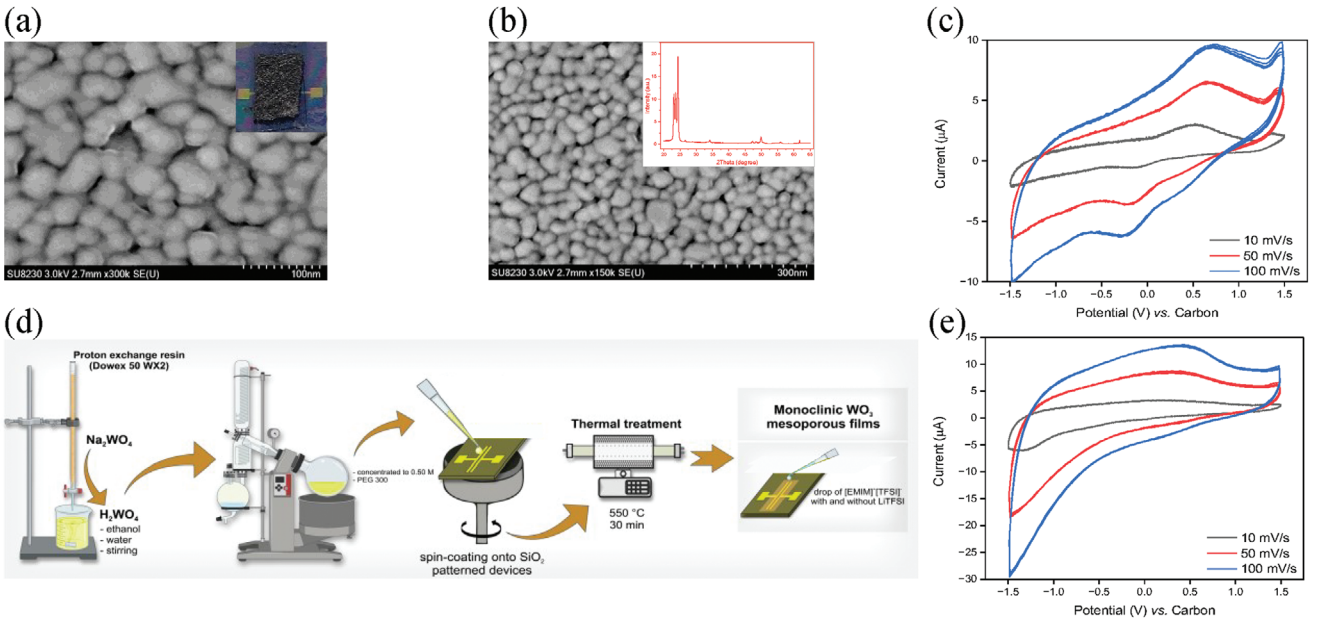

Figure 2. SEM images of a nanostructured WO_3 thin film obtained at a) 300 000x (insert: three terminals WO_3-based IGT), b) 150 000x (inset: XRD patterns of the WO_3 film). CV results for spin-coated WO_3-IGTs with at c) [EMIM][TFSI]-gated, e) 0.1 mol L^{-1} LiTFSI in [EMIM][TFSI]-gated, illustrating different scan rates (blue line: 100 mV s^{-1}, red line: 50 mV s^{-1}, black line: 10 mV s^{-1}). d) Schematic diagram depicting the preparation of the monoclinic WO_3 porous film via a solution-based method and its deposition onto gold-silicon patterned devices.

Interestingly, the 2D histograms collected in 0.1 mol L^{-1} LiTFSI in [EMIM][TFSI] exhibited less well-resolved patterns, with clear separation observed only in the first ionic layer (Figure 1f).

The results were further analyzed using histograms of separations, providing clearer visualization of the peak positions and statistical distribution of the ionic layers at the selected spots. Results obtained with [EMIM][TFSI] in five different spots at the IGT channel, under V_{gs} = 1 V bias (Figure 1g), indeed exhibited discernible peaks attributed to the first four ionic layers, with the position of the first ion layer at 0.54 ± 0.09 nm. In the case of 0.1 mol L^{-1} LiTFSI in [EMIM][TFSI], only the peak related to the first ionic layer could be resolved, positioned at 0.73 ± 0.07 nm (Figure 1h). These results indicate that the first layer at the WO_3/IL interface without Li^+ is relatively closer to the surface compared to when Li^+ is present. Another significant difference related to the characteristics of the first layer peak was the value observed for the full width at half maximum (FWHM), a parameter related to the degree of ion ordering.[38] For the IL without Li^+, an FWHM value of 0.53 ± 0.01 nm was observed, whereas with Li^+ it is 0.85 ± 0.07 nm. Therefore, the sharper peaks observed in the IL without Li^+ suggest that the first $[EMIM]^+$ layer is much more ordered and compact compared to the layering of both $[EMIM]^+$ and Li^+. The absence of peaks related to subsequent layers in the presence of Li^+ further indicates the disordered nature of the ionic arrangement in the Li^+-rich ionic media.

2.4. Transistor Characterization

Transfer and output characterization of WO_3-based IGT with [EMIM][TFSI] (**Figure 3a–c**) and 0.1 mol L^{-1} LiTFSI in [EMIM][TFSI] (Figure 3d–f) as gating media shows n-type semiconductor behavior. In the transfer characteristics, we observe that the I_{ds} increases as V_{gs} scan rate decreases from 100 to 10 mVs^{-1} in both ionic media, due to the increased time available to accommodate ion movement. The approximately threefold increase in I_{ds} modulation observed for the WO_3 IGT gated with 0.1 mol L^{-1} LiTFSI in [EMIM][TFSI] is attributed to the additional charge injection via the electrochemical doping process through the Li^+/e^- double injection mechanism.

2.5. Synaptic Behaviors and Response Time of WO_3-Based IGTs

Synaptic IGT responses to input voltage pulses are essential properties for mimicking various types of plasticity observed in neural synapses. We examined changes in response time and I_{ds} current amplitude under the application of V_{gs} pulses with varied pulse amplitudes, pulse frequencies, number of pulses, and pulse durations.

2.5.1. Spike Amplitude-Dependent Plasticity (SADP) Influenced by the Gating Medium

An increase in I_{ds} replicates the EPSC observed in biological neurons, enabling the implementation of artificial synapses. **Figure 4a,b** demonstrates SADP, illustrating the tuning of synaptic plasticity through V_{gs} spike amplitude. We recorded I_{ds} peaks induced by various V_{gs} amplitudes (0.8, 1, 1.5, and 2 V), all maintained at a duration of 4 s and a V_{ds} of 1.2 V. We observe I_{ds} peak increases with V_{gs} pulse amplitude in both [EMIM][TFSI] and 0.1 mol L^{-1} LiTFSI in [EMIM][TFSI]-gated WO_3-based IGTs. The

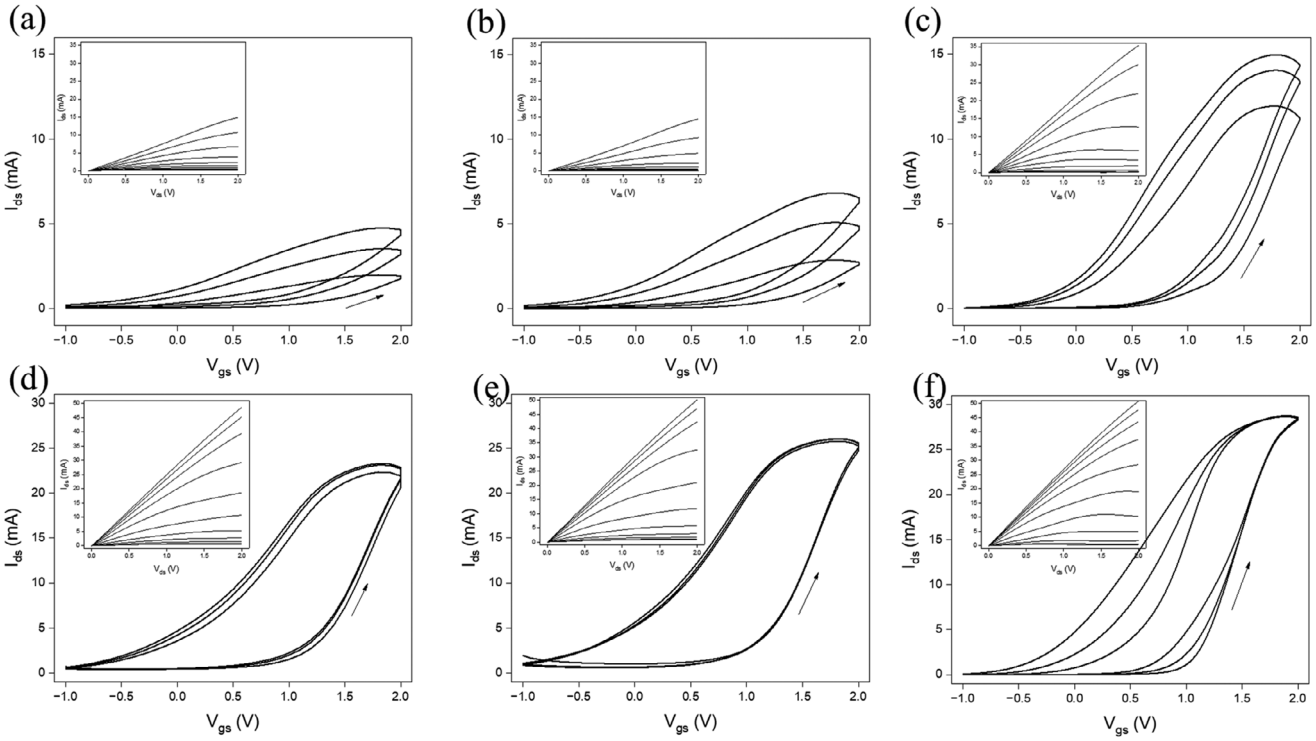

Figure 3. Transfer characteristics of WO_3-based IGT in the linear regime (V_{ds} = 1.2 V, (3 cycles)) at V_{gs} scan rates 100, 50, 10 mVs^{-1} at a–c) [EMIM][TFSI]-gated, d–f) 0.1 mol L^{-1} LiTFSI in [EMIM][TFSI]-gated (inset: output characteristics of WO_3 based IGT with V_{gs} = [0:0.2:2] V at V_{ds} scan rates 100, 50, and 10 mVs^{-1} at a–c) [EMIM][TFSI]-gated, d–f) 0.1 mol L^{-1} LiTFSI in [EMIM][TFSI]-gated).

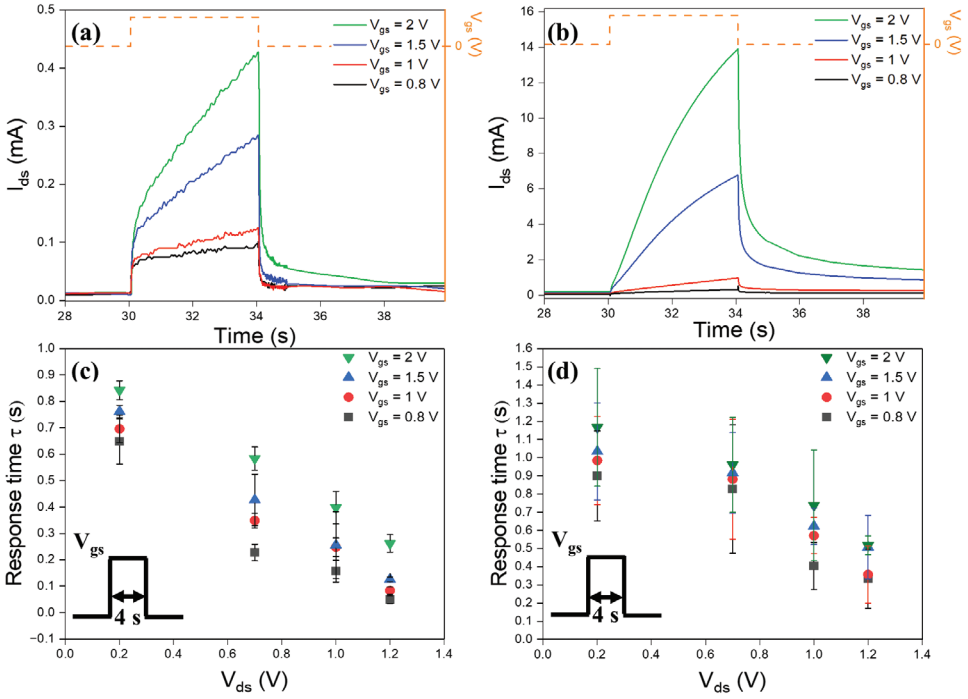

Figure 4. a) Spike amplitude-dependent plasticity (SADP) of WO_3 IGTs, showing EPSC (I_{ds} pulses) responses to V_{gs} pulses with varying amplitudes (V_{gs} = 0.8, 1, 1.5, and 2 V), all with a duration of 4 s and V_{ds} = 1.2 V, gated by a) [EMIM][TFSI] b) 0.1 mol L^{-1} LiTFSI in [EMIM][TFSI]. Response time c) [EMIM][TFSI]-gated WO_3 based IGT d) 0.1 mol L^{-1} LiTFSI in [EMIM][TFSI]-gated WO_3 based IGT in response to different V_{gs} pulses (0.8, 1, 1.5, and 2 V) and V_{ds} values (0.2, 0.7, 1, and 1.2 V), with a pulse duration of 4 s.

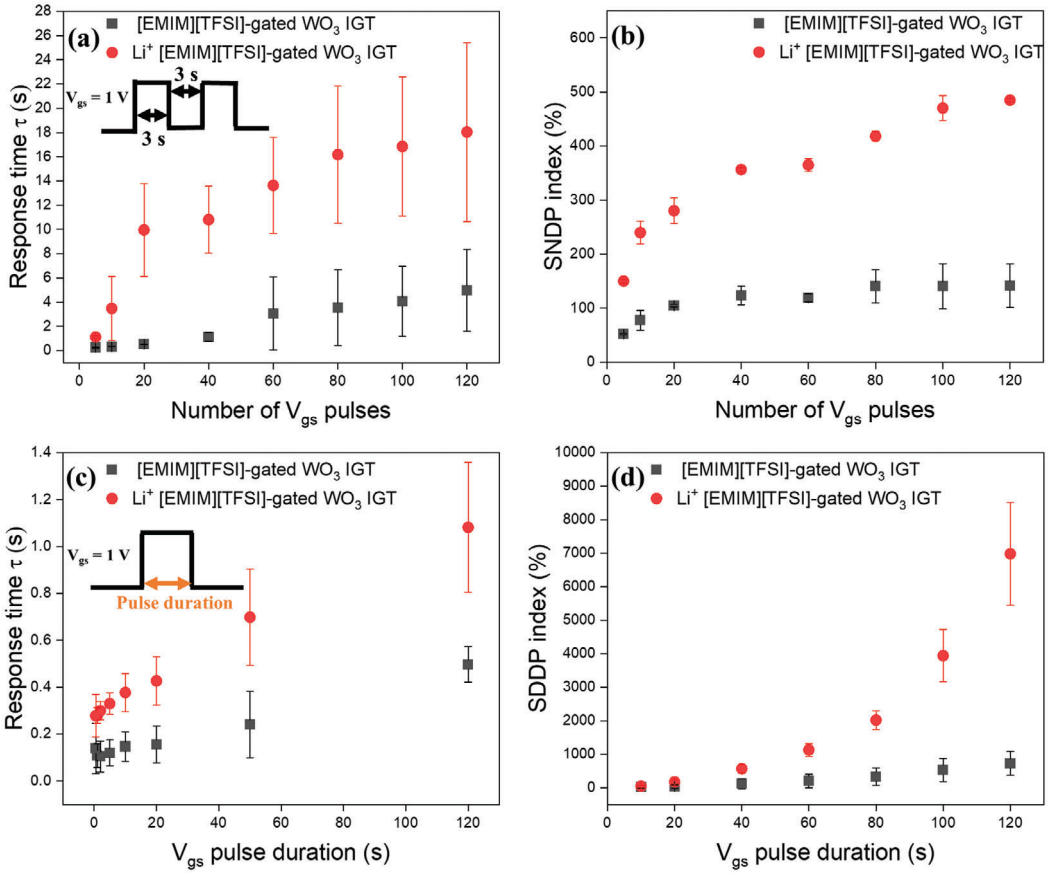

Figure 5. Synaptic behavior of artificial synapses for 0.1 mol L^{-1} LiTFSI in [EMIM][TFSI] and [EMIM][TFSI] gated WO_3 IGT. a) Response time of WO_3 IGT versus different numbers of square step train V_{gs} pulses, from 5 to 120 pulses. V_{gs} and V_{ds} = 1 V. b) SNDP index as a function of the number of V_{gs} pulses, V_{gs} and V_{ds} = 1 V. c) Response time of WO_3 IGT versus V_{gs} pulse duration. d) SDDP index as a function.

variation in I_{ds} is significantly greater in the presence of Li^+, with the I_{ds} peak in 0.1 mol L^{-1} LiTFSI in [EMIM][TFSI]-gated WO_3-based IGTs being 3–30 times higher than that in [EMIM][TFSI]-gated WO_3-based IGTs under applied V_{gs} values ranging from 0.8 to 2 V. This transition STP to LTP, achieved through careful selection of the gating medium, results from the augmented electrochemical doping of the channel due to the intercalation of Li^+ within the WO_3 film lattice. After V_{gs} pulses are removed, I_{ds} start to decay, exhibiting varying response times. Both types of transistors exhibit an increase in response time with higher V_{gs} and lower V_{ds} (Figure 4c,d).

The 0.1 mol L^{-1} LiTFSI in [EMIM][TFSI]-gated WO_3-based IGT exhibits a slower response time and maintains higher I_{ds} peaks compared to the [EMIM][TFSI]-gated device, mimicking the long-term synaptic weight modulation seen in biological synapses (long-term plasticity, LTP).

This slower response time is achieved by introducing Li^+ from the ionic medium into the WO_3 channel of the IGT. Li^+ can penetrate the WO_3 lattice more deeply than the larger $[EMIM]^+$. When positive V_{gs} is removed, Li^+ diffuses back from the WO_3 lattice to the ionic medium over a longer duration than $[EMIM]^+$, leading to a slower response time (Figure 4c,d). The errors observed in the results, derived from experiments conducted on three WO_3-based transistors.

2.5.2. Spike Number-Dependent Plasticity (SNDP) Influenced by the Gating Medium

To investigate the impact of incorporating Li^+ on LTP in WO_3-based IGTs, we applied V_{gs} pulse trains. Successive stimuli contribute to the gradual modulation of electrical conductance or synaptic weight, a phenomenon known as SNDP, calculated as $(I_{dsn} - I_{ds1}) / I_{ds1} \times 100\%$, where n represents the number of V_{gs} pulses. **Figure 5b** shows the SNDP index behavior in both [EMIM][TFSI]-gated and 0.1 mol L^{-1} LiTFSI in [EMIM][TFSI]-gated WO_3-based IGTs, where we applied 5, 10, 20, 40, 60, 80, 100, and 120 consecutive V_{gs} = 1 V pulses with a constant V_{ds} = 1 V, a pulse duration and interval of 3 s.

Two major differences were observed between the two types of transistors. First, the [EMIM][TFSI]-gated transistor exhibited a faster response time than the other type following V_{gs} pulse trains, as shown in Figure 5a. The increasing number of pulses leads to deeper insertion of Li^+ into the WO_3 lattice, resulting in a prolonged de-doping process and a slower response time. Second, the SNDP index of the [EMIM][TFSI]-gated IGT, as shown in Figure 5b, exhibited saturation with an increasing number of V_{gs} pulses; this saturation was not observed in the presence of Li^+, thus indicating the difference in the change of channel conductance between the two different gating media of WO_3-based

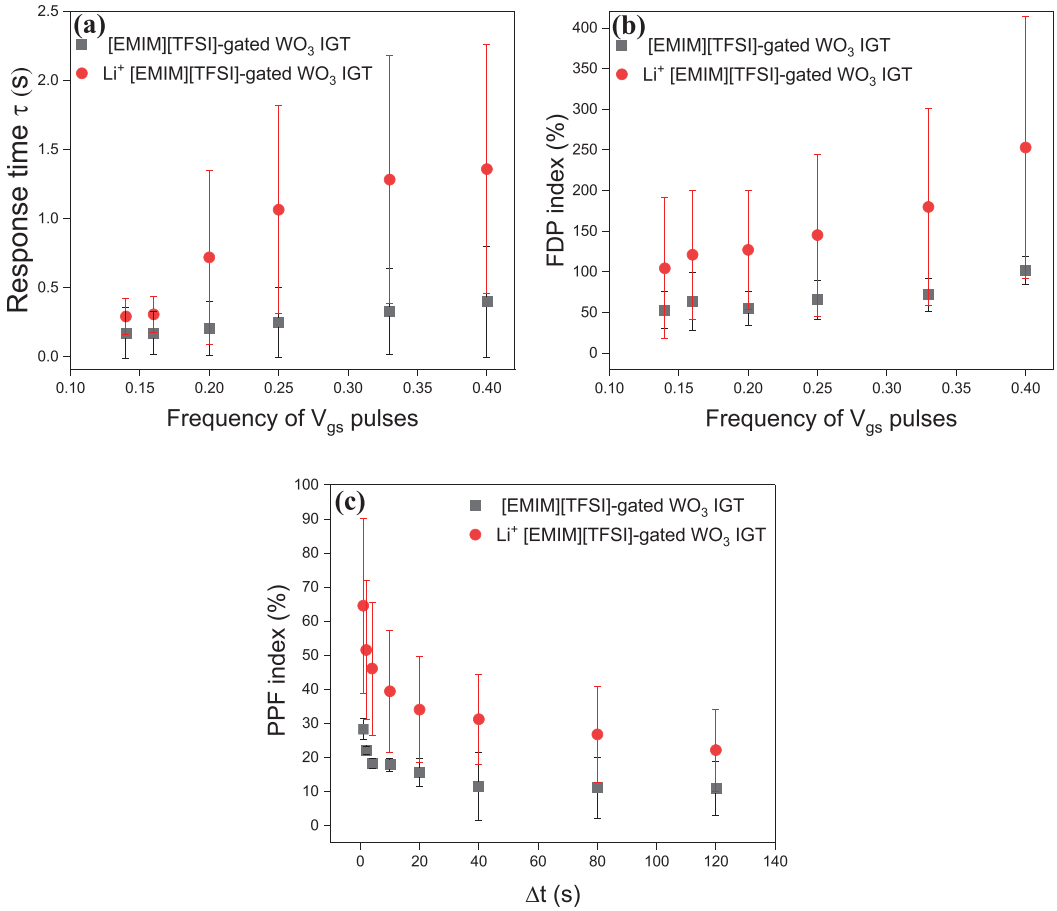

Figure 6. a) Response time versus V_{gs} pulse frequency for 0.1 mol L^{-1} LiTFSI in [EMIM][TFSI] and [EMIM][TFSI] gated WO_3 IGT. b) FDP index as a function of the frequency of V_{gs} pulses. c) PPF index after applying two consecutive V_{gs} = 1 V pulses versus Δt, the time interval of pulses.

IGTs. These differences in conductance changes became more pronounced after 100 to 120 consecutive pulses. Therefore, it can be concluded from Figure 5a,b that the transition from STP to LTP in the artificial synapse is highly dependent on the number of V_{gs} pulses, especially in the presence of Li^+.

2.5.3. Spike Duration-Dependent Plasticity (SDDP) Influenced by the Gating Medium

When V_{gs} pulses with pulse durations of 10 s or shorter were applied, both [EMIM][TFSI]-gated and 0.1 mol L^{-1} LiTFSI in [EMIM][TFSI]-gated WO_3 based IGTs exhibited STP behavior, as shown in Figure 5c. However, if the pulse duration is applied for more than 50 s, IGTs start to show LTP.

Figure 5d shows the SDDP diagrams in the WO_3 artificial synapse exclusively in dependence on two input parameters: gating medium and pulse duration. During the SDDP index measurement shown in Figure 5d, we increase the pulse duration from 0.5 to 120 s. We varied the gating medium from [EMIM][TFSI]-gated IGT to 0.1 mol L^{-1} LiTFSI in [EMIM][TFSI]-gated IGT are measured under $V_{gs} = 1$ and $V_{ds} = 1$. With increasing pulse duration in both IGTs, the response time increases, although we can see a much slower response time in the presence of Li^+. Lithiation can cause a delay in de-doping time and increase τ.

2.5.4. Frequency-Dependent Plasticity (FDP) Influenced by the Gating Medium

The FDP synaptic behavior we study here refers to a characteristic of the IGT artificial synapse, where the synaptic weight (conductance state) changes not only with the duration of the applied V_{gs} pulse but is also strongly related to the variation of V_{gs} time interval within each spike cycle of presynaptic spike trains. To measure the effect of FDP we apply the train of 10 V_{gs} pulses with an amplitude of 1 V, the same duration time of 2 s, and frequency of 0.14, 0.16, 0.2, 0.25, 0.33, 0.4 Hz to [EMIM][TFSI]-gated and 0.1 mol L^{-1} LiTFSI in [EMIM][TFSI]-gated WO_3 IGT. The FDP index demonstrates that as the frequency of the presynaptic spike (V_{gs}) train increases, I_{ds} gradually increases for both types of IGTs with different gating media. **Figure 6b** illustrates the frequency-dependent I_{ds} gain, which is calculated as FDP = $(I_{ds10} - I_{ds1})/I_{ds1}$ × 100%, where I_{ds10} and I_{ds1} represent the 10th and 1st I_{ds} values, respectively. The FDP gain increases from 53% to 101% as the frequency rises from 0.14 to 0.4 Hz for the [EMIM][TFSI]-gated WO_3-IGT. In comparison, the presence of Li^+ in the

gating medium leads to a more pronounced enhancement of the FDP index, increasing from 104% to 253% over the same frequency range. Figure 6a shows the response time of WO_3-IGT as a function of V_{gs} frequency, where an increase in response time with rising frequency is observed. At higher V_{gs} frequencies (with the same number of spikes), more ions penetrate the channel, leading to longer redistribution times and slower response. The presence of Li^+ in the gating medium further extends the redistribution time, making it longer than that of the [EMIM][TFSI]-gated IGT (Figure 6a).

2.5.5. Paired-Pulse Facilitation (PPF)

Paired-pulse facilitation (PPF) is known for decoding temporal information in auditory and visual signals. We investigated PPF behavior and compared them between [EMIM][TFSI]-gated and 0.1 mol L^{-1} LiTFSI in [EMIM][TFSI]-gated WO_3-IGT. PPF behavior was induced by applying a pair of identical V_{gs} pulses (1 V, 4 s), with varying interval time (Δt), (1, 2, 4, 10, 20, 40, 80, 120 s) as shown in Figure 6c (PPF = $\Delta I_{ds}/I_{ds1} \times 100\%$). We observed that the I_{ds} change induced by the second pulse is greater than that caused by the first. This increase in conductance (facilitation) is attributed to ion insertion into the channel during the first pulse, while the second pulse was applied before the ions had fully diffused back into the ionic medium. As a result, I_{ds} increased after the second pulse due to higher ion concentration in the channel. In the presence of Li^+, the I_{ds} increase induced by the second pulse is greater than that observed in IGTs without Li^+ in the system. In this case, the delithiation of WO_3 takes more time after the removal of the first V_{gs} pulse, allowing I_{ds} to experience a greater increase with the application of the second V_{gs} pulse. The highest PPF index of 72% was achieved in the 0.1 mol L^{-1} LiTFSI in [EMIM][TFSI]-gated IGT, while the PPF index for the [EMIM][TFSI]-gated IGT was 32%. The PPF index was found to decrease as the interval time increased. This decrease occurs because longer intervals between pulses allow ions to relax back into the ionic medium, thereby diminishing the effect.

3. Conclusion

In conclusion, this study successfully demonstrates the fabrication and detailed characterization of a WO_3-based ion-gated synaptic transistor tailored for neuromorphic computing applications. By using [EMIM][TFSI] and 0.1 mol L^{-1} LiTFSI in [EMIM][TFSI] as gating media, we systematically investigate the material and transistor characteristics, revealing significant insights into their behavior and performance.

AFM FD profiling and CV analyses provide a comprehensive understanding of the EDL structure and electrochemical properties. The combined experiments suggest that the less ordered and less compact EDL at the IL/MO interface layer in 0.1 mol L^{-1} LiTFSI in [EMIM][TFSI] results from Li^+ being present inside the channel bringing about electrochemical doping. On the other hand, in WO_3 IGT gated with pure [EMIM][TFSI], there is evidence that the interface-confined unconventional doping and electrostatic effect leads to a higher degree of organization of the EDL and clearly-defined voltammetric peaks. The differences between the dominance of faster electrostatic/interface-confined and slower electrochemical doping processes (which include ionic transport) significantly impact conductance modulation and time response to different bias signals in the neuromorphic devices using the two gating media. Notably, the presence of Li^+ in the gating medium enhances the device performance, as evidenced by a threefold increase in I_{ds} in the transfer curves. This enhancement is attributed to Li^+ intercalation, which enhances conductivity while affecting the device's response time.

The synaptic behavior observed in the WO_3-based IGTs, including STP, LTP, SADP, SNDP, SDDP, FDP, and PPF, demonstrate that these devices can effectively mimic key neural synapse functions, highlighting their potential in neuromorphic systems. These findings underscore the importance of ionic medium selection in optimizing the synaptic transistor response time, current amplifying, and transition between STP and LTP, paving the way for the development of energy-efficient and high-performance neuromorphic systems capable of adaptive learning and real-time processing.

Overall, our study highlights the promise of WO_3-based IGTs in advancing intelligent systems, emphasizing their potential to replicate the dynamic and adaptive functionalities of biological synapses, thereby contributing to the future of neuromorphic computing. Future work will focus on further optimizing material properties and exploring other ionic compositions to enhance the synaptic behavior and overall performance of these promising WO_3-based IGTs. To further emulate the timescales of biological synapses, reducing pulse durations and fine-tuning device performance will be necessary. Additionally, while WO_3 thin films exhibit excellent stability under ambient conditions, encapsulation will be considered to ensure long-term device reliability and stability.

4. Experimental Section

Preparation of WO_3 Films: A solution-based method was used to prepare the WO_3 thin films (Figure 2d).[1] Specifically, tungstic acid (H_2WO_4) was prepared by passing 20 mL of a 0.5 mol L^{-1} Na_2WO_4 aqueous solution through proton-exchange resin (Dowex 50WX2, 100–200 mesh). The resin was previously preconditioned in 50 mL of 1 mol L^{-1} H_2SO_4 for 30 min and washed several times with deionized water (DIW) to achieve a pH of 7. The eluted solution was collected in 16 mL of ethanol under continuous magnetic stirring to slow down the condensation. Subsequently, the solution's volume was reduced under low pressure and heating to achieve a concentration of ≈0.5 mol dm^{-3}. As an organic stabilizer, 4 mL of PEG-300 was added to the freshly evaporated stirred solution (WO_3/PEG-300 ratio of ≈0.5 w/w). A viscous, pale yellowish precursor solution (under continuous stirring) was stored in dark conditions before precipitation and used to fabricate WO_3 films for no more than three days. The precursor was spin-coated onto the device surface. The deposition involved drop-casting 40 µL and spinning at 4000 rpm for 40 seconds. The deposited layer was dried at room temperature for 10 min and subsequently annealed in a tubular furnace (under flowing oxygen) at 550 °C for 30 min.

Fabrication of the IGT Device: WO_3 films were used on SiO_2/Si substrates as transistor channel materials of [EMIM][TFSI]- gated IGTs. The SiO_2/Si substrates were photolithographically patterned with source and drain electrodes (40 nm-thick Au and 5 nm-thick Ti adhesion layer). The interelectrode distance, L, was 10 µm and the electrode width was W = 4 mm. For the photolithography, the Si substrate was spin-coated with AZ 900 MIR positive photoresist, baked, and exposed to UV light through a photomask, to define the desired geometry for the electrode pattern. Post-exposure baking and development revealed the patterned areas, which

were then coated with a thin layer of Ti (5 nm) for adhesion, followed by Au (40 nm), via e-beam evaporation. Finally, the excess metal was removed using a lift-off process, leaving Ti/Au electrodes in the desired pattern. Before WO_3 film deposition, substrates were sequentially ultrasonically cleaned with isopropyl alcohol, acetone, and isopropyl alcohol (10 min each), then exposed to UV–Ozone for 15 min. Before use, the ionic liquid [EMIM][TFSI] (from IoLiTec, with a purity of over 99%) was purified under vacuum conditions of $\approx 10^{-5}$ Torr for 24 h at 60 °C and then was dropped on a DuraporeR membrane, typically 4 mm × 9 mm in size and 125 µm thick, positioned in alignment with the transistor channel. To prepare an alternative gating medium, 0.1 mol L^{-1} LiTFSI in [EMIM][TFSI] for applying on the membrane, bis(trifluoromethane)-sulfonimide lithium salt (LiTFSI, Sigma–Aldrich, 99.95%) was dissolved in purified [EMIM][TFSI] until Li^+ concentration of 0.1 mol L^{-1} was achieved. The gate, along with the reference/counter electrode, was composed of a high surface area carbon paper (Spectracarb 2050), measuring 6 mm × 3 mm and 170 µm in thickness. This was coated with an ink formulated from activated carbon (PI-CACTIF SUPERCAP BP10, Pica, at a concentration of 28 mg mL^{-1}) and a polyvinylidene fluoride (PVDF, KYNAR HSV900, at a concentration of 1.4 mg mL^{-1}) binder, all in N-methyl pyrrolidone (NMP, sourced from Fluka).

Materials Characterization: AFM, SEM, and XRD were employed to investigate the WO_3 film under ambient conditions. The AFM images were acquired in semi-contact (tapping) mode using an NSG10 cantilever with specific dimensions (length: 95 µm, width: 30 µm, resonant frequency: 240 kHz, and force constant: 11.8 N/m) utilizing an NT-MDT NTEGRA II microscope. Additionally, the structure of WO_3 films was analyzed via XRD using a Bruker D8 instrument with a Cu-Kα source (wavelength: 1.54 Å). The film thickness was determined using a profilometer (Dektak 150). SEM images were obtained using a Hitachi SU-8230 Cold Field Emission Scanning Electron Microscope (CFE-SEM), which has an electron source size of 5 nm, and an energy spread ranging from 0.2 to 0.3 eV.

Electrical and Electrochemical Characterizations of WO_3-IGT: In an N_2 glovebox with H_2O and O_2 concentrations below 3 ppm, electrical and electrochemical characterizations were conducted. Transistor characteristics were analyzed using an Agilent B1500A semiconductor parameter analyzer in a custom electrical probe station. Cyclic voltammetry measurements were taken with a VersaSTAT4 potentiostat.

AFM FD profiles were collected using a Cypher AFM from Asylum Research (Oxford Instruments, UK) using the Cypher droplet holder and TR800 PB (Olympus) probes with a nominal spring constant of 0.61 N/m. A droplet of purified [EMIM][TFSI] or 0.1 mol L^{-1} LiTFSI in [EMIM][TFSI] was added to the devices. The FD curves were collected with a ramp distance of 30 nm and a ramp rate of 0.5 Hz. To control the drain-source and gate-source electrical bias (electrical measurements), an SP-300 two-channel potentiostat (Biologic) was used.

Acknowledgements

Research funded by Air Force Office of Scientific Research (AFOSR/SOARD, USA) under award number FA9550-23-1-0575. AFM was conducted as part of a user project at the Center for Nanophase Materials Sciences (CNMS), which is a US Department of Energy, Office of Science User Facility at Oak Ridge National Laboratory (User project CNMS2023-A-01765). C.S. acknowledges NSERC (Discovery Grant) and the Canada Research Chairs for financial support. LCdSN acknowledges the financial support of FAPESP (2022/03553-0), CAPES-PROEX and CNPq (304899/2023-2). LPC thanks to Coordenação de Aperfeiçoamento de Pessoal de Nível Superior (CAPES) for the Doctorate scholarship and Emerging Leaders of Americas Program (ELAP), support of Global Affairs Canada.

Conflict of Interest

The authors declare no conflict of interest.

Data Availability Statement

The data that support the findings of this study are available from the corresponding author upon reasonable request.

Keywords

ion gated transistors, ion gating media, ion intercalation, neuromorphic computing, synaptic plasticity, synaptic transistors, WO_3 films

Received: October 22, 2024
Revised: December 17, 2024
Published online: March 20, 2025

[1] N. Zins, Y. Zhang, C. Yu, H. An, in *Frontiers of Quality Electronic Design (QED): AI, IoT and Hardware Security*, (Ed.: A. Iranmanesh), Springer International Publishing, Cham **2023**, 259–296.
[2] D. Ivanov, A. Chezhegov, D. Larionov, *Frontiers in Neuroscience* **2022**, *16*, 959626.
[3] M. Dragoman, D. Dragoman, in *Atomic-Scale Electronics Beyond CMOS*, Springer International Publishing, Cham **2021**, 187–213.
[4] M. Zolfagharinejad, U. Alegre-Ibarra, T. Chen, S. Kinge, W. G. van der Wiel, *The European Phy. J. B* **2024**, *97*, 70.
[5] S. Reardon, *Nature* **2018**, *26*.
[6] S. Choi, J. Yang, G. Wang, *Adv. Mater.* **2020**, *32*, 2004659.
[7] D. Marković, A. Mizrahi, D. Querlioz, J. Grollier, *Nat. Rev. Phys.* **2020**, *2*, 499.
[8] A. J. Edwards, G. Krylov, J. S. Friedman, E. G. Friedman, *Neuromorphic Comput. Engineer.* **2024**, *4*, 014005.
[9] Y. Sun, H. Wang, D. Xie, *Nano-Micro Lett.* **2024**, *16*, 211.
[10] K. Roy, A. Jaiswal, P. Panda, *Nature* **2019**, *575*, 607.
[11] H. Han, H. Yu, H. Wei, J. Gong, W. Xu, *Small* **2019**, *15*, 1900695.
[12] S. Jiang, S. Nie, Y. He, R. Liu, C. Chen, Q. Wan, *Mater. Today Nano* **2019**, *8*, 100059.
[13] K.-T. Chen, J.-S. Chen, *Appl. Phys. Lett.* **2022**, *121*, 19.
[14] G. Li, M. Dai, Y. Zhang, *Adv. Electron. Mater.* **2022**, *8*, 2101003.
[15] R. Karimi Azari, T. Lan, C. Santato, *J. Mater. Chem. C* **2023**, *11*, 8293.
[16] P. Monalisha, A. P. Kumar, X. R. Wang, S. Piramanayagam, *ACS Appl. Mater. Interfaces* **2022**, *14*, 11864.
[17] Y. Park, M.-K. Kim, J.-S. Lee, *J. Mater. Chem. C* **2021**, *9*, 5396.
[18] X. Li, B. Yu, B. Wang, L. Bao, B. Zhang, H. Li, Z. Yu, T. Zhang, Y. Yang, R. Huang, *Nanoscale* **2020**, *12*, 16348.
[19] P. Subin, A. Asha, K. Saji, M. Jayaraj, *J. Mater. Sci.: Mater. Electron.* **2021**, *32*, 13051.
[20] R. Karimi Azari, Z. Gao, A. Carrière, C. Santato, *RSC Applied Interfaces* **2024**, *1*, 564.
[21] K. Hadiyal, R. Ganesan, A. Rastogi, R. Thamankar, *Sci. Rep.* **2023**, *13*, 7481.
[22] C. G. Granqvist, *Sol. Energy Mater. Sol. Cells* **2000**, *60*, 201.
[23] A. Ponzoni, E. Comini, G. Sberveglieri, J. Zhou, S. Z. Deng, N. S. Xu, Y. Ding, Z. L. Wang, *Appl. Phys. Lett.* **2006**, *88*, 203101.
[24] Y. Li, Y. Yao, L. Wang, L. Wang, Y. Pang, Z. Luo, S. Arunprabaharan, S. Liu, Q. Zhao, *Sci. China Technol. Sci.* **2024**, *67*, 1040.
[25] G. V. D. O. Silva, A. Subramanian, X. Meng, S. Zhang, M. S. Barbosa, B. Baloukas, D. Chartrand, J. C. Gonzáles, M. O. Orlandi, F. Soavi, F. Cicoira, C. Santato, *J. Phys. D: Appl. Phys.* **2019**, *52*, 305102.
[26] X. Meng, F. Quenneville, F. Venne, E. Di Mauro, D. Işık, M. Barbosa, Y. Drolet, M. M. Natile, D. Rochefort, F. Soavi, *J. Phys. Chem. C* **2015**, *119*, 21732.

[27] J. R. H. Garza, L. P. Camargo, R. K. Azari, L. C. da Silva Neres, S. Khaleel, M. S. Barbosa, F. Soavi, C. Santato, *J. Mater. Chem. C* **2024**, *12*, 2416.
[28] J. Rivnay, P. Leleux, M. Ferro, M. Sessolo, A. Williamson, D. A. Koutsouras, D. Khodagholy, M. Ramuz, X. Strakosas, R. M. Owens, C. Benar, J.-M. Badier, C. Bernard, G. G. Malliaras, *Sci. Adv.* **2015**, *1*, 1400251.
[29] Y. Cui, Q. Wang, G. Yang, Y. Gao, *J. Solid State Chem.* **2021**, *297*, 122082.
[30] J. T. Yang, C. Ge, J. Y. Du, H. Y. Huang, M. He, C. Wang, H. B. Lu, G. Z. Yang, K. J. Jin, *Adv. Mater.* **2018**, *30*, 1801548.
[31] B. Park, Y. Hwang, O. Kwon, S. Hwang, J. A. Lee, D.-H. Choi, S.-K. Lee, A. R. Kim, B. Cho, J.-D. Kwon, *ACS Appl. Mater. Interfaces* **2022**, *14*, 53038.
[32] R. D. Nikam, M. Kwak, J. Lee, K. G. Rajput, H. Hwang, *Adv. Electron. Mater.* **2020**, *6*, 1901100.
[33] E. J. Fuller, F. E. Gabaly, F. Léonard, S. Agarwal, S. J. Plimpton, R. B. Jacobs-Gedrim, C. D. James, M. J. Marinella, A. A. Talin, *Adv. Mater.* **2016**, *29*, 0895J.
[34] J. Zhou, C. Wan, L. Zhu, Y. Shi, Q. Wan, *IEEE Electron Device Lett.* **2013**, *34*, 1433.
[35] K. Liang, R. A. Matsumoto, W. Zhao, N. C. Osti, I. Popov, B. P. Thapaliya, S. Fleischmann, S. Misra, K. Prenger, M. Tyagi, *Adv. Funct. Mater.* **2021**, *31*, 2104007.
[36] N. Agmon, *J. Am. Chem. Soc.* **2017**, *139*, 15068.
[37] M. S. Barbosa, N. Balke, W.-Y. Tsai, C. Santato, M. O. Orlandi, *J. Phys. Chem. Lett.* **2020**, *11*, 3257.
[38] J. M. Black, M. Zhu, P. Zhang, R. R. Unocic, D. Guo, M. B. Okatan, S. Dai, P. T. Cummings, S. V. Kalinin, G. Feng, *Sci. Rep.* **2016**, *6*, 32389.